AIAA 2003-5104

RSRM and ETM03 Internal Flow Simulations and Comparisons

R. A. Ahmad, R.A. Morstadt and A.M. Eaton
ATK Thiokol Propulsion Corp.
Brigham City, UT

39th AIAA/ASME/SAE/ASEE Joint Propulsion Conference and Exhibit
July 20-23, 2003
Huntsville, AL

RSRM and ETM03 Internal Flow Simulations and Comparisons

Rashid A. Ahmad,[+] R.A. Morstadt[*] and A.M. Eaton[**]
Motor Performance Department, Gas Dynamics Section
Science and Engineering
ATK Thiokol Propulsion Corp., Brigham City, Utah 84302

ETM03 (Engineering Test Motor-03) is an extended length RSRM (Reusable Solid Rocket Motor) designed to increase motor performance and create more severe internal environments compared with the standard four-segment RSRM motor configuration. This is achieved primarily through three unique design features. First is the incorporation of an additional RSRM center segment, second is a slight increase in throat diameter, and third is the use of an Extended Aft Exit Cone (EAEC). As a result of these design features, parameters such as web time, action time, head end pressure, web time average pressure, maximum thrust, mass flow rate, centerline Mach number, pressure and thrust integrals have all increased compared with nominal RSRM values. In some cases these increases are substantial. The primary objective of the ETM03 test program is to provide a platform for RSRM component margin testing. Test results will not only provide direct data concerning component performance under more adverse conditions, but serve as a second design data point for developing, validating and enhancing component analytical modeling techniques. To help component designers assess how the changes in motor environment will affect performance, internal flow simulations for both the nominal RSRM and ETM03 motor designs were completed to obtain comparisons of aero-thermal boundary conditions and system loads. Full geometries for both motors were characterized with two-dimensional axi-symmetric models at burn times of 1, 20, 54, 67 and 80-seconds. A sixth set considered burn times of 110 and 117-seconds for RSRM and ETM03, respectively. The simulations were performed using the computational fluid dynamics (CFD) commercial code FLUENT.® Of particular interest were any differences between the two motor environments that could lead to a significant increase in system loads, or in internal insulation and/or nozzle component charring and erosion in ETM03 compared with RSRM. Based on these comparative analyses conducted in this study, the objective of ETM03 will be achieved by providing a more adverse operating environment for motor components than the nominal RSRM environment. For example: Higher chamber pressure drop in ETM03 than in RSRM; higher centerline Mach numbers approaching the nozzle in ETM03 than in RSRM; higher heat transfer rates for the internal insulation and nozzle components in ETM03 than in RSRM; and higher levels of droplet impingement and slag accumulation in ETM03 than in the RSRM.

Nomenclature

A	area, m^2 (ft^2)
a	empirical constant (Eq. 3b)
C_p, C_v	specific heats at constant pressure and volume, respectively, J/kg-K (Btu/lb_m-R)
d	diameter, m (in.)
h	convective heat transfer coefficient, W/m^2-K (Btu/hr-ft^2-R)
κ, ε	turbulence kinetic energy (m^2/s^2 (ft^2/s^2)) and its rate of dissipation ($m^2/s^2/s$ ($ft^2/s^2/s$)), respectively
k	gas thermal conductivity, W/m-K (Btu/hr-ft-R)
MW	molecular weight, kg/kgmole (lb/lbmole)
M	Mach number
M_d	mass fraction of particles with diameter greater than d_p
N	particles spread diameter
N_p	number of particles
n	burning rate pressure exponent
P_o, P	total and static pressure, respectively, Pa (psia)
Pr	*Prandtl* number
$\dot{q}''$	wall heat flux, W/m^2 (Btu/hr-ft^2)
$\dot{r}_p$	propellant burn rate, m/s (ft/s)
$\dot{R}_p''$	rate of accretion flux, kg/m^2-s (lbm/ft^2-s)
r	radius, m (in.)
S	source term (Eq. 1)
T_o, T	total and static temperature, respectively, K (R)
u, v	axial and radial velocity components, m/s (ft/s)
x, y	axial and radial axes, m (in.)
y^+	non-dimensional distance from the wall in wall units
α	augmentation/deaugmentation factor
γ	ratio of specific heats, C_p/C_v
μ, ν	dynamic (N-s/m^2 (lb_m/ft-s)) and kinematic (m^2/s (ft^2/s)) viscosity, respectively
ρ	gas density, kg/m^3 (lb_m/ft^3)
(x), (y)	function of axial and radial directions, respectively

Subscripts

e	at nozzle exit
f	face
DP	discrete phase
g	gas
o	chamber conditions
p	particles, propellant
s	static, smoke
w	wall

[+] Sr. Principal Engineer, Associate Fellow AIAA, [*] Sr. Principal Engineer, Sr. Member AIAA, [**] Supervisor, Gas Dynamics.

Superscripts

$*$ throat conditions

' flux

– mean and time averaged

Introduction

ETM03 is an extended length RSRM designed to increase motor performance and create more severe internal environments compared with the standard four-segment motor configuration. This is achieved primarily through four unique design features. First is the incorporation of an additional RSRM center segment, second is a 2.25-inch increase in throat diameter, third is the use of an Extended Aft Exit Cone (EAEC), and fourth, propellant corners have been modified to have 3 by 24 in. propellant chamfers. The EAEC was previously tested on FSM-05 as an RSRM enhancement, although it was never implemented as part of the flight baseline configuration. As a result of these design features, parameters such as web time, action time, head end pressure, web time average pressure, maximum thrust, mass flow rate, centerline Mach number, pressure and thrust integrals have all increased compared with nominal RSRM values. In some cases these increases are substantial.

The primary objective of the ETM03 test program is to provide a platform for RSRM component margin testing. Test results will not only provide direct data concerning component performance under more adverse conditions, but serve as a second design data point for developing, validating and enhancing component analytical modeling techniques. These data can also be used to support a Five Segment Booster (FSB) development program should the shuttle program choose to pursue this option for abort mode enhancements during the ascent phase.

To help component designers assess how the changes in motor environment will affect performance, internal flow simulations for both the nominal RSRM and ETM03 motor designs were completed to obtain comparisons between aero-thermal boundary conditions and system loads. Full geometries for both motors were characterized with two-dimensional axi-symmetric models at burn times of 1, 20, 54, 67 and 80-seconds. A sixth set considered burn times of 110 and 117-seconds for RSRM and ETM03, respectively. For this initial set of predictions, a 3 by 6 in. chamfer was a feature of the grain design on the forward end of each propellant segment. The 1 s burn time geometry for the RSRM and ETM03 are shown in Figs. 1 and 2, respectively. The simulations were performed using the computational fluid dynamics (CFD) commercial code FLUENT.® Of particular interest were any differences between the two motor environments that could lead to a significant increase in system loads, or in internal insulation and/or nozzle component charring and erosion in ETM03 compared with RSRM.

The burn times of 1, 20, and 80 sec post ignition simulations were repeated for ETM03 with 3 by 24 in. propellant chamfers. The results were compared and contrasted against ETM03 with 3 by 6 in. propellant chamfers. The 1 sec burn time was selected because that is the point in time with the maximum chamber pressure drop and the greatest potential for propellant deformation. The 20 s was selected because it is the point in time with the maximum mass flow rate and maximum thrust, and the 80 s burn time was selected as a representative for showing any differences in slag collection/accretion when the propellant has burned out of the aft-end.

Discussion of Modeling Approach

All the simulation involved a two-dimensional axi-symmetric model of the full motor and the grain at different burn times.

Governing equations, operating conditions and thermo-physical properties, grids, boundary conditions, turbulence modeling, computational schemes, numerical convergence (residuals), convective heat transfer, two-phase modeling, and vacuum thrust and specific impulse are discussed next.

Governing Equations: The numerical studies considered the solution of the steady-state Navier-Stokes equations, energy equation, the turbulence kinetic energy with its rate of dissipation equations, and the necessary constitutive equations (ideal gas law, power law for gas thermal conductivity and viscosity, etc.). The general governing equation was

$$\nabla . \left(\rho \bar{V} \phi - \Gamma_\phi \nabla \phi\right) = S_\phi \qquad (1)$$

and the mass conservation equation

$$\nabla . \left(\rho \bar{V}\right) = 0 \qquad (2)$$

where ϕ can be velocity components (u, v, w), enthalpy (i), turbulence quantities (κ, ε), and species concentrations (C); Γ is an exchange coefficient for ϕ; S_ϕ is a source term for ϕ per unit volume.

Operating Conditions and Thermo-physical Properties: Table 1 summarizes operating conditions and thermo-physical properties. Table 2 summarizes the particles thermo-physical properties and distribution.

Grids: Coarse grids with quadrilateral cells used in this simulation and are summarized in Table 1. All the grids for 1, 54, 80, 110 and 117 s burn times were generated using GRIDGEN[2] and made orthogonal and smoothed from one domain to another. Grids for 20 and 67 s burn times were generated using GAMBIT[3].

Boundary Conditions: the boundary conditions in this simulation are as follows:

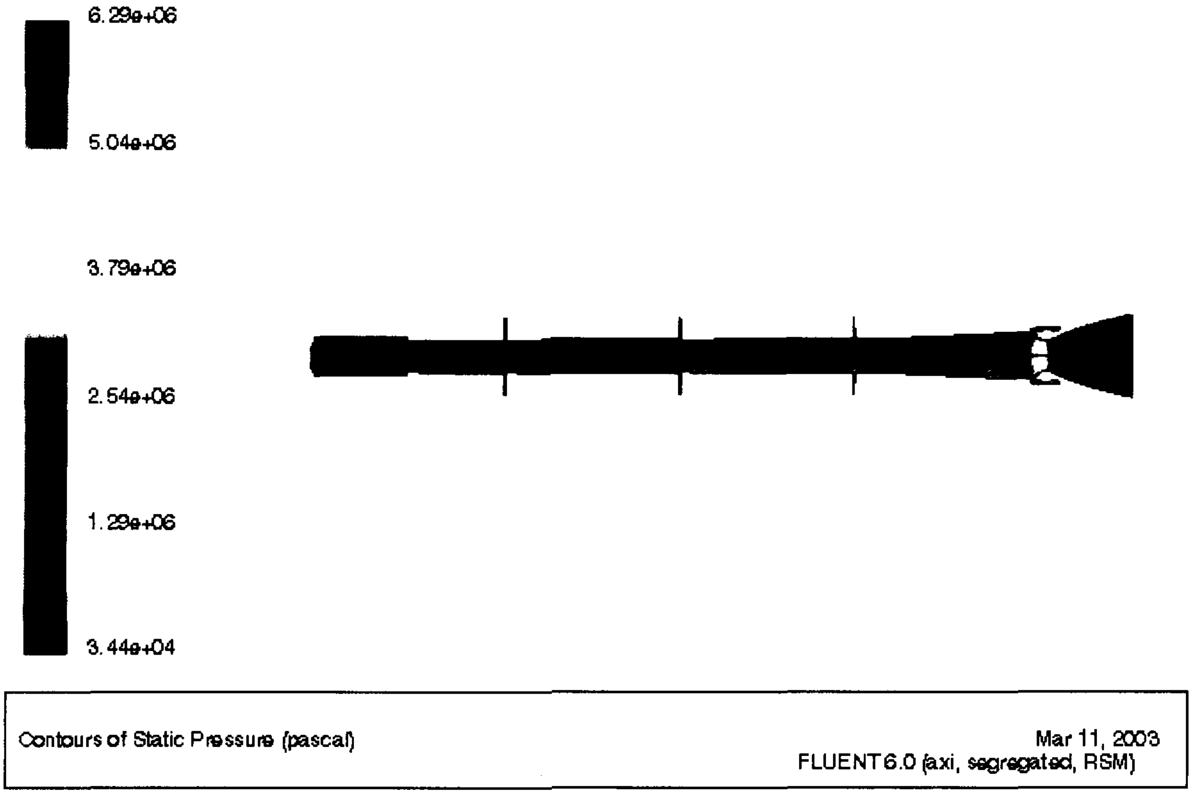

Fig. 1 RSRM local static pressure distribution at 1 s post ignition.

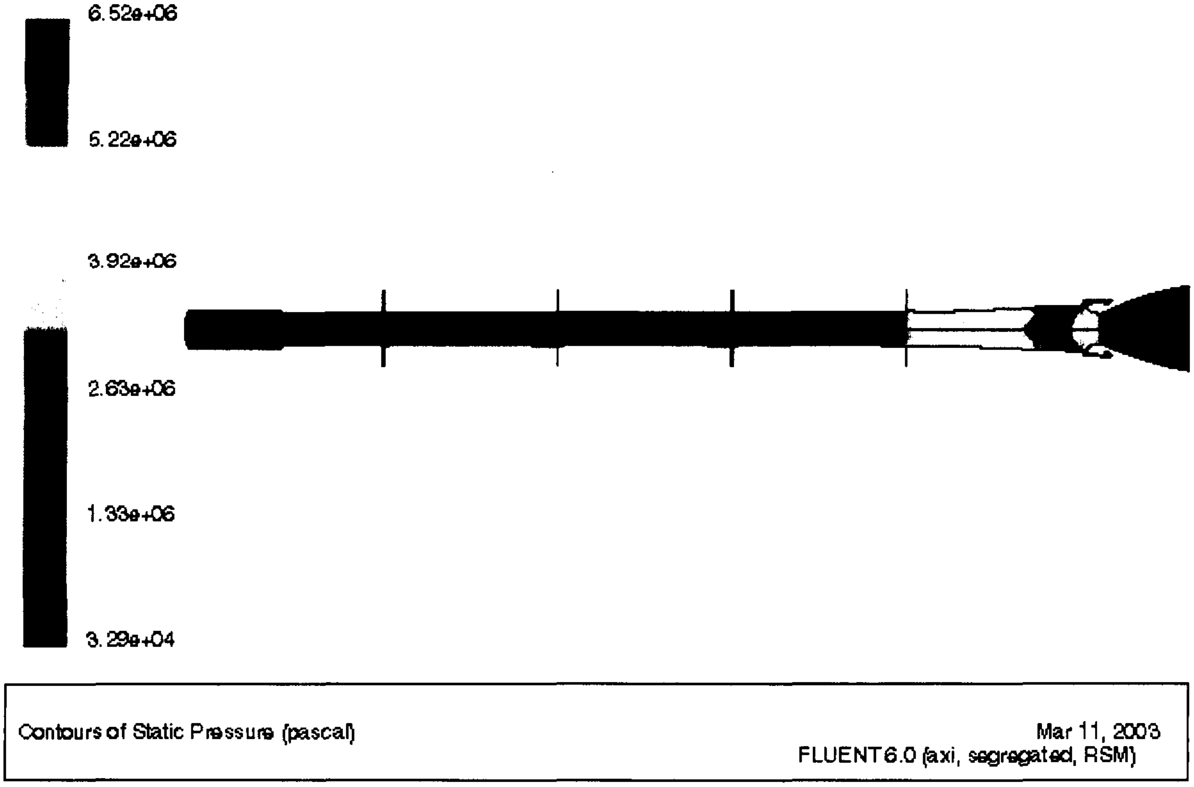

Fig. 2 ETM03 local static pressure distribution at 1 s post ignition.

Table 1 Operating ballistic head-end pressure used to run NASA-Lewis program[1] to obtain chamber temperature and gas properties

Burn time	**1 s**		**20 s**		**54 s**		**67 s**		**80 s**		**110 s**	**117 s**
Motor	**RSRM**	**ETM-03**	**RSRM**	**ETM-03**	**RSRM**	**ETM-03**	**RSRM**	**ETM-03**	**RSRM**	**ETM-03**	**RSRM**	**ETM-03**
P_o (MPA, psia)	6.274, 910.78	6.262, 908.3	6.029, 874.5	6.014, 872.2	4.123, 597.98	4.684, 679.43	4.336, 628.9	4.803, 696.6	4.317, 626.162	4.922, 713.938	2.814, 408.17[a]	2.404, 348.697[a]
T_o (K, R)	3424.76, 6164.56	3419.00, 6154.20	3418.00, 6152.4	3418.00, 6152.4	3384.50, 6092.10	3395.30, 6111.54	3384.00, 6091.2	3397.00, 6114.6	3388.40, 6099.12	3399.40, 6118.92	3351.30, 6032.34	3337.20, 6006.96
μ_o (N-s/m^2, lbm/ft-s)	9.25×10^{-5}, 6.22×10^{-5}	9.25×10^{-5}, 6.22×10^{-5}	9.64×10^{-5}, 6.48×10^{-5}, (b)	9.64×10^{-5}, 6.48×10^{-5}, (b)	9.19×10^{-5}, 6.17×10^{-5}	9.21×10^{-5}, 6.19×10^{-5}	9.58×10^{-5}, 6.44×10^{-5}, (b)	9.58×10^{-5}, 6.44×10^{-5}, (b)	9.19×10^{-5}, 6.18×10^{-5}	9.21×10^{-5}, 6.19×10	9.13×10^{-5}, 6.13×10^{-5}	9.10×10^{-5}, 6.12×10^{-5}
C_p (J/kg-K, Btu/lbm-R)	1966.54, 0.47	1966.54, 0.47	1965, 0.469	1965, 0.469	1964.45, 0.469	1965.28, 0.469	1964, 0.469	1972, 0.471	1964.87, 0.469	1965.28, 0.469	1963.29, 0.469	1963.19, 0.469
k_o (W/m-K, Btu/hr-ft-R)	0.396, 0.229	0.396, 0.229	0.3685[a], 0.213	0.3624[a], 0.209	0.394, 0.228	0.395, 0.228	0.3624[a], 0.209	0.3624[a], 0.209	0.394, 0.228	0.395, 0.228	0.392, 0.227	0.391, 0.226
MW (kg/kgmole, lbm/lbmole)	28.465	28.464	28.473	9.64×10^{-5}	28.350	28.386	28.363	28.363	28.363	28.399	28.242	28.196
γ	1.1746	1.1746	1.1750	1.1750	1.1756	1.1753	1.1756	1.1753	1.1755	1.1752	1.1766	1.1770
Cells	98,650	105,850	54,125	63,012	76,080	89,440	69,090	77,409	65,780	76,040	84,500	100,700

Nozzle exit inadvertently shortened slightly, D_o is taken at propellant tip closest to nozzle nose-cap tip, $\rho_p = 1.009$ kg/m^3 (0.063 lb$_m$/in^3), $P_{o,ref} = 4.309$ MPa (625 psia)

RSRM: $r_{p,ref} = 0.368$ in./s (0.935 cm/s), $n = 0.35$, $\rho_p\, a = 0.07765$ kg$^{0.65}$ m$^{-1.65}$ s$^{-0.3}$

ETM03: $r_{p,ref} = 0.343$ in./s (0.871 cm/s), $n = 0.32$, $\rho_p\, a = 0.11445$ kg$^{0.68}$ m$^{-1.68}$ s$^{-0.36}$

[a]: At this burn time, the chamber pressure in the RSRM is higher than in ETM03. The reverse is true for all other burn times.
(b): $k = k_o\,(T/T_{ref})^n = 0.3624\,(T/3400)^{0.6656}$

Table 2 Summary of particle thermo-physical properties and distribution

Properties		**Rosin-Rammler Distribution**		**Uniform Distribution**	
ρ_s(kg/m^3, lbm/ft^3)	1601.85, 100	D_{min} (micron)	10	D_p (micron)	11.68
$C_{p,s}$ (J/kg-K, Btu/lbm-R)	1800.32, 0.43	D_{max} (micron)	600		
k_s (W/m-K, Btu/hr-ft-R)	10.47, 6.05	$D_{average}$ (micron)	87.8		
Equivalent MW (kg/kgmole, lbm/lbmole)	26.07	Spread	1.1426		
		N_p	8		

1) ***At the propellant surface:*** Mass flux was calculated as a function of the local static pressure as

$$\dot{m}'' = \alpha \rho_p a \left[P_S(x,y)\right]^n \quad (3a)$$

Where

$$a = \dot{r}_{ref} \Big/ \left(P_{o,\,ref}\right)^n \quad (3b)$$

The total pressure given in Table 1 along with propellant formulation was used as input to the NASA-Lewis program[1] to obtain chamber gas temperature (T_o), dynamic viscosity (μ_o), specific heat at constant pressure (C_p), thermal conductivity (k_o), and molecular weight. They are given in Table 1. The local gas dynamic viscosity and thermal conductivity were calculated locally as a function of local temperature as

$$\mu = \mu_o \left(T \big/ T_o\right)^{\varsigma} \quad (4a)$$

and

$$k = k_o \left(T \big/ T_o\right)^{\varsigma} \quad (4b)$$

where the exponent ζ is calculated from the NASA-Lewis program[1].

In addition, propellant density, reference pressure, reference burn rate and its exponent are also given. Turbulence intensity of 5% and hydraulic diameter were specified. The augmentation factor, α, was used as 1 for the propellant except in the head end fin region, where it was increased to 4.528 to account for the three-dimensional fins modeled in two-dimensional axi-symmetric analysis.

2) ***Wall Boundary Conditions:***

Thermal Boundary Conditions: Fig. 3 shows the specified surface temperature used as thermal boundary condition, respectively. The surface temperature profile along the converging-diverging section of the nozzle was curve-fitted using TableCurve2D[4] as

$$T_W = \frac{a + cx + ex^2 + gx^3 + ix^4 + kx^5}{1 + bx + dx^2 + fx^3 + hx^4 + jx^5} \quad (5)$$

where x was taken along the nozzle surface and where the coefficients are given as follows: a = 2789.03, b = - 4.61, c = -13307.21, d = 11.96, e = 32905.45, f = - 6.33, g = -20712.33, h = - 0.916, j = 1174.06 and k = 815.51. The correlation coefficient was calculated to be r^2 = 0.997. A user defined function (UDF) was used to compile the specified surface temperature profile. The submerged wall (nosecap and cavity) was assumed to be isothermal at 2750K (4950R).

It is to be noted that the repeated legend in the figures was added for the purpose of representing the corresponding English units on the right-hand ordinate. Therefore, the first and last legend are expected to represent two curves falling on the top of each other.

Velocity Boundary Conditions: No slip condition was specified at walls.

3) ***At exit:*** A supersonic boundary condition was utilized where the quantities (P, T, u, v, κ, ε) were calculated from cells upstream of the exit. The exit pressure, temperature, turbulence intensity, and exit hydraulic diameter were specified to start the calculation. The exit pressure and temperature were updated as the solution proceeded.

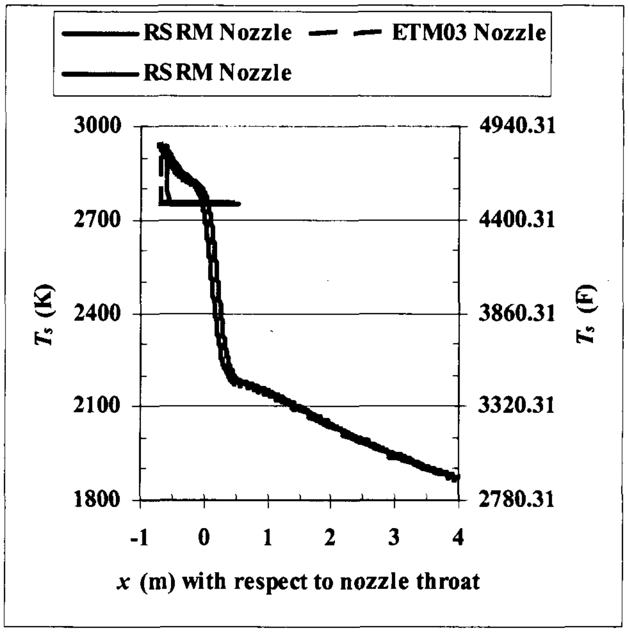

Fig. 3 RSRM and ETM03 nozzle specified surface temperatures.

Turbulence Modeling: Two turbulence models were used in the simulations: standard κ-ε and RNG κ-ε with standard wall function for near wall treatment. The three burn times of 1, 20 and 80 s post ignition were also modeled using an alternative turbulence model called Reynolds stress model (RSM). This model has been found to better predict motor pressure drop than the RNG κ-ε or the standard κ-ε turbulence models. In addition, there is no need to limit the turbulence viscosity ratio or alter any default turbulence constants.

Computational Schemes: The segregated solver in the commercial code Fluent[5] was used. Differencing schemes utilized were 1st and 2nd order Upwind, Power law, and Quick schemes. The 1st Upwind scheme was used to start the problem and the higher order schemes to obtain the final results. The 2nd order Upwind and Quick schemes were found to give similar results in terms of mass flow rate and mass imbalance, head-end pressure, chamber pressure drop, and maximum Mach number at the nozzle exit. Power law scheme was found to converge the best and fastest.

Numerical Convergence (Residuals): Numerical convergence was achieved by satisfying four requirements in the following sequence. First, the residual error diminished as the number of iterations was increased. Second, the profiles of the variables ceased to change, at least qualitatively. Third, a first monitor on the total pressure at the propellant surface until the average total pressure ceased to change. Fourth, a second monitor on the mass imbalance between the inlet (propellant surface) and the outlet (nozzle exit) mass flow rates until it reached a small value (10^{-3} – 10^{-5} kg/s).

Convective Heat Transfer: The ratio of the convective heat transfer coefficient to the specific heat at constant pressure (h/C_p) was calculated as

$$\frac{h(x)}{C_P} = \frac{\dot{q}''_W(x)}{C_P\left[T_o - T_W(x)\right]} \tag{6}$$

This ratio is usually used as input in the CMA code[6] for nozzle erosion predictions.

Two-Phase Modeling: The two phases are continuous phase (combustion gas) and a discrete phase (aluminum oxide droplets (Al_2O_3 or slag)). Since droplet agglomeration/breakup was not modeled, they were assumed spherical and of a constant size distribution anywhere in the motor and were injected at propellant surface.

Two diameter distribution models are needed. They are the Rosin-Rammler[5] and a uniform diameter distribution. The first yields better results in the motor chamber where particles have less propensity to break up. The uniform diameter distribution model yields better results in the nozzle where particles would break up in a highly accelerated flow. The present results are limited to the Rosin-Rammler distribution and is explained next.

Rosin-Rammler Diamater Distribution Model: The particle size and distribution used in this study were based on investigation[7] into the effects of ingredient property variation on RSRM TP-H1148 production propellant. Aluminum oxide is the total fraction of aluminum (*Al*) that is converted to large Al_2O_3 discrete phase particles ($d_p \geq$ 10 μm) after combustion is complete and was taken[8] as:

$$\dot{m}_{Alumina} = 0.29\,\dot{m} \tag{7a}$$

The non-aluminum oxide gas which may be considered as smoke is therefore

$$\dot{m}_S = \dot{m} - \dot{m}_{Alumina} = 0.71\,\dot{m} \tag{7b}$$

The discrete phase (*DP*) portion of the total particulate population (Alumina) was taken as

$$\dot{m}_{DP} = \dot{m}_{AL_2O3} = 0.29\,\dot{m}_{Alumina} = 0.084\,\dot{m} \tag{7c}$$

However, the mass flow rate of the continuous phase (*CP*) was increased to include the small smoke-like particles in the CP as follows:

$$\dot{m}_{CP} = \dot{m} - \dot{m}_{DP} = 0.916\,\dot{m} \tag{7d}$$

Inert particles density, specific heat at constant pressure and thermal conductivity are given in Table 2. The equivalent molecular weight of the gas was calculated as

$$MW = \frac{18.76 + 7.58\,f_s}{0.926} \tag{7e}$$

where f_s is the ratio of mass flow rate of smoke to the total mass flow rate and is taken as 0.71, i.e.

$$f_s = \dot{m}_S / \dot{m} = 0.71 \tag{7f}$$

The equivalent molecular weight is in Table 2.

Particle size distribution for the alumina included in the discrete phase was defined by fitting the size distribution to the Rosin-Rammler equation[5] (Chap. 14). In this approach, the complete range of particle sizes was divided into a set of discrete size ranges, each to be defined by a single stream that was part of the group. The particle size data obeys the distribution shown in Fig. 4 and was curve-fitted in this study as

$$M_{d_p} = 1.015\exp\left(-d_p/86.565\right) \tag{7g}$$

with a coefficient of determination of 0.99. The particle diameter (d_p) is to be specified in microns.

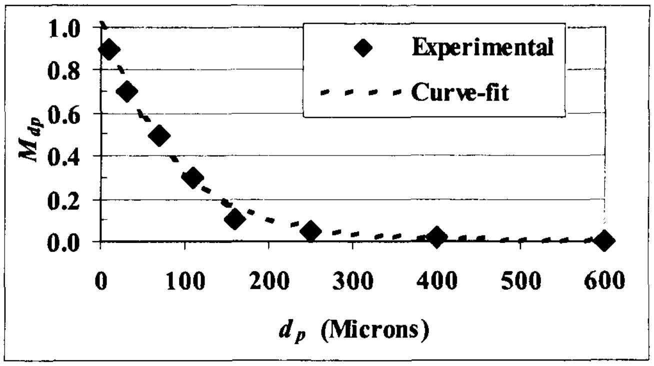

Fig. 4 Rosin-Rammler curve for particle size distribution.

The Rosin-Rammler distribution function is based on the assumption that an exponential relationship exists between the particle diameter, (d_p), and the mass fraction of particles with diameter greater than d_p, M_{dp} as

$$M_{d_p} = \exp\left[-\left(\frac{d_p}{\bar{d}_p}\right)^N\right] \tag{7h}$$

where $\bar{d}_p$ is the mean diameter and N is the spread parameter. The average diameter was obtained by noting that the value of d_p at which $M_{dp} = \exp(-1) = 0.368$. From the above figure, the average diameter was 87.53 µm. The numerical value of the spread parameter was calculated from the above relationship as

$$N = \frac{\ln\left(-\ln M_{dp}\right)}{\ln\left(\frac{d_p}{\bar{d}_p}\right)} \tag{7i}$$

Upon substituting the values, an average value for N was calculated to be 1.1426. In summary, 8 discrete particle sizes ranging from 10 to 600 microns with a mean diameter of 87.80 µm and a spread parameter of 1.1428 were specified and given in Table 2.

The Al_2O_3 rate of accretion flux along a wall is defined[5] as:

$$\dot{R}'' = \sum_{p=1}^{N_p} \dot{m}_p \Big/ A_{w,f} \tag{7j}$$

The walls of the submerged region and nozzle were set as trap walls for particles upon impact as boundary conditions. Propellant surface was set as a reflecting surface for particles. Particles at the exit plane were set to escape. Particle concentration is a flow quantity that exists in the flow field and at the wall. The particle trajectories and their local Al_2O_3 concentrations are of interest to understand the submerged region and nozzle environments in terms of insulation performance and possibly Al_2O_3 slag rate of accretion flux or accumulation.

RESULTS

The CFD results of these analyses include comparisons of calculated performance parameters for the RSRM and ETM03 at 6 burn times. In some cases, results are limited to 1 s post ignition for brevity and clarity.

Figures 1 and 2 show the RSRM and ETM03 geometry considered and the static pressure distribution in the whole motor at 1 s post ignition. Maximum static pressures were calculated at the motor head end and were 6.29 MPa (912.29 psia) and 6.25 MPa (906.49 psia), respectively. The maximum pressure in the ETM03 still higher even though the nozzle throat diameter has been enlarged. As burn time progresses, the internal gas flow geometry changes based on the burn rate.

Figures 5 and 6 show the static pressure and the Mach number at the motor centerline. Here the chamfer is defined by 7.72 cm (3 in.) rise and 15.24 cm (6 in.) run.

The following is a comparison of performance parameters between CFD calculations vs. ballistic predictions. Figure 7 shows the RSRM and ETM03 calculated head end pressures using CFD in this study in comparison with ballistic predictions. Similarly, Fig. 8 shows the RSRM and ETM03 calculated motor chamber pressure drop in this study in comparison with measured values of the FSM-9 test motor. At 1 s post ignition, the chamber pressure drop in the FSM-9 was measured to be 167 psia. At 1 s post ignition, the RSRM chamber pressure drop was calculated to be 175 psia, yielding a difference of about 8 psia. As burn time increases, the agreement between measured and CFD calculations of chamber pressure drop improves. An obvious reason is the three-dimensional effects contributed by the fins at the head end at early burn times. This study involved two-dimensional axi-symmetric analyses.

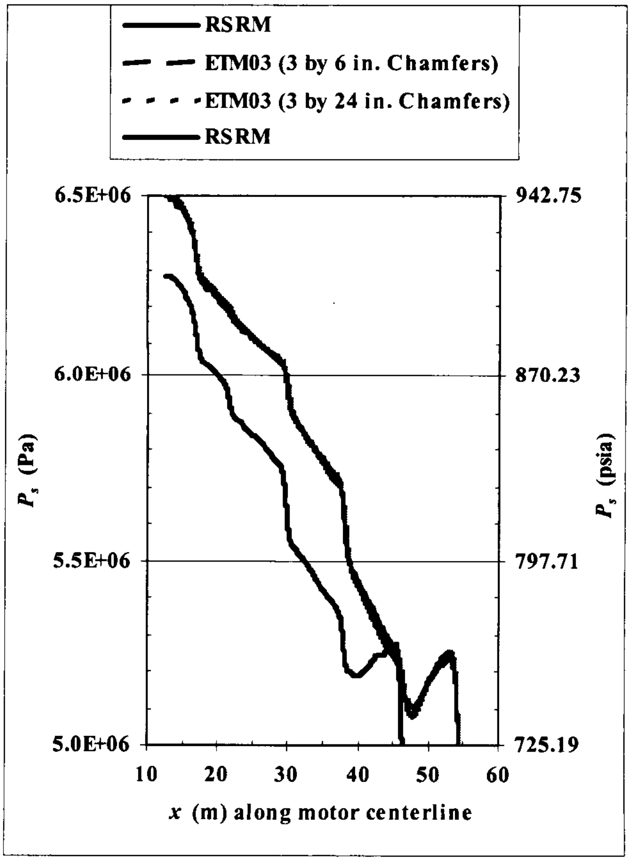

Fig. 5 RSRM and ETM03 motor chamber pressure drops at 1 s post ignition.

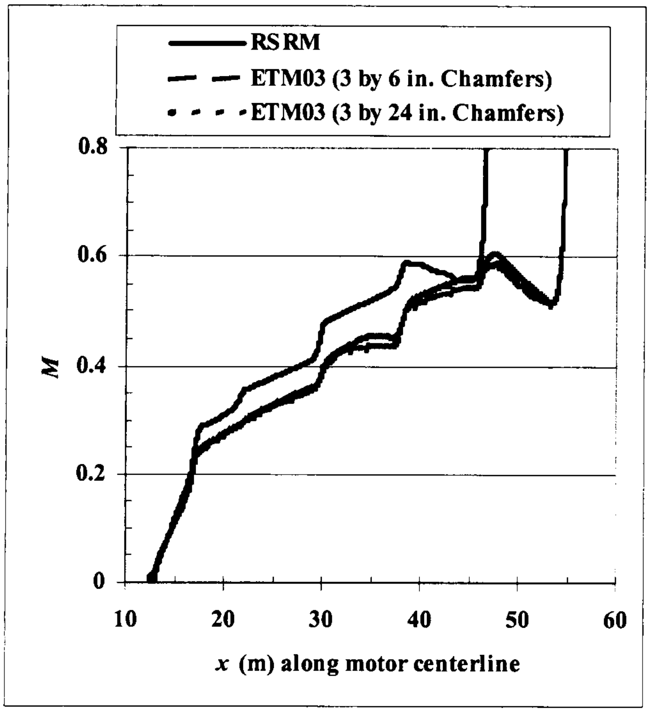

Fig. 6 RSRM and ETM03 motor chamber Mach numbers at 1 s post ignition.

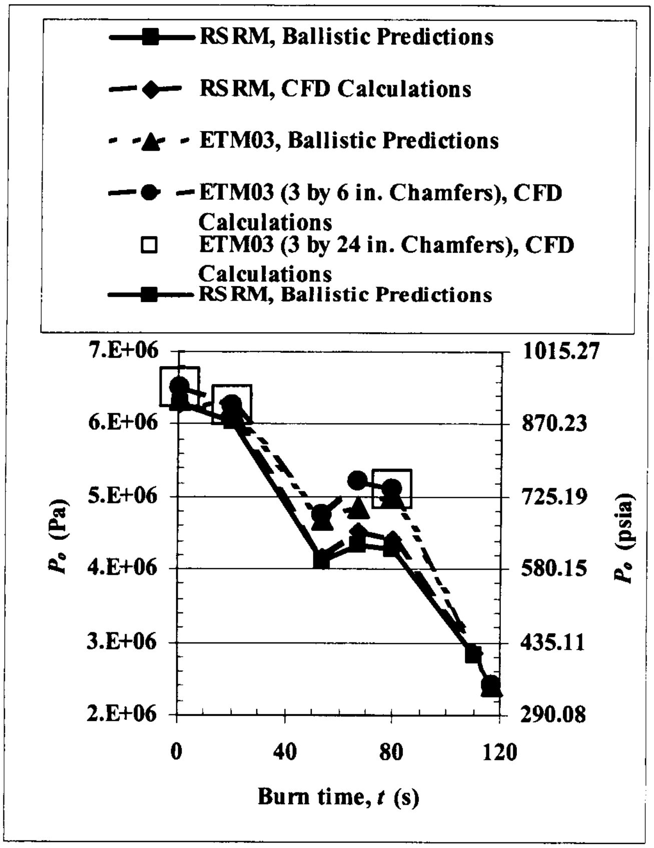

Fig. 7 RSRM and ETM03 head end pressures.

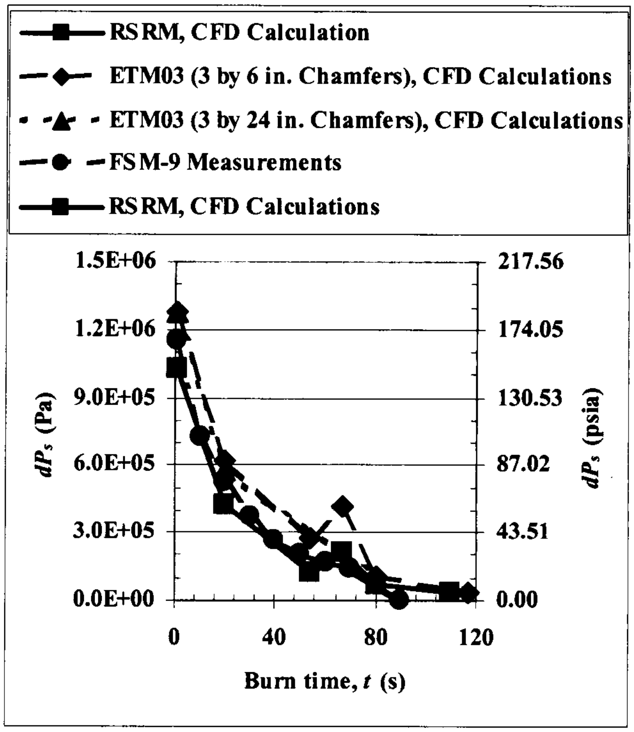

Fig. 8 RSRM and ETM03 chamber pressure drops.

The following results pertain to wall values: Figures 9, 10 and 11 show the local values of wall total pressure, ratio of heat transfer coefficient to the specific heat at constant pressure, and wall y^+. The first, is important for system loads. The second, is important in aero-thermal boundary conditions. The third, verifies whether gridding is consistent with turbulence modeling. They are between 25 and 350 which are consistent with turbulence wall treatment.

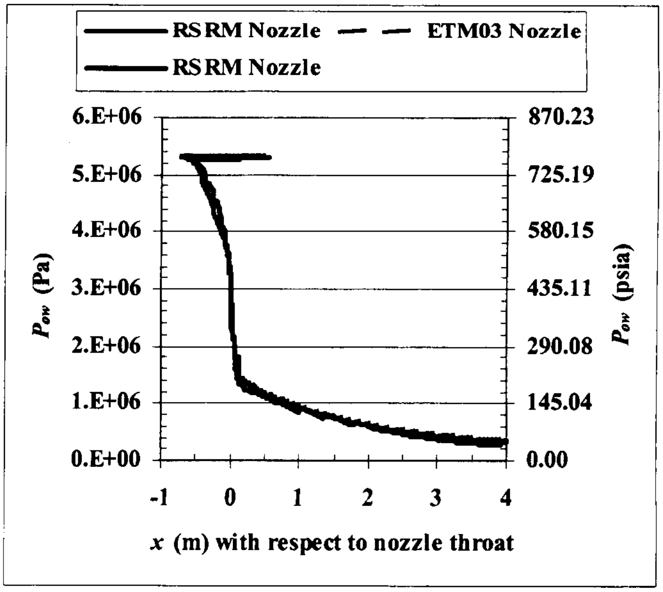

Fig. 9 RSRM and ETM03 wall total pressures.

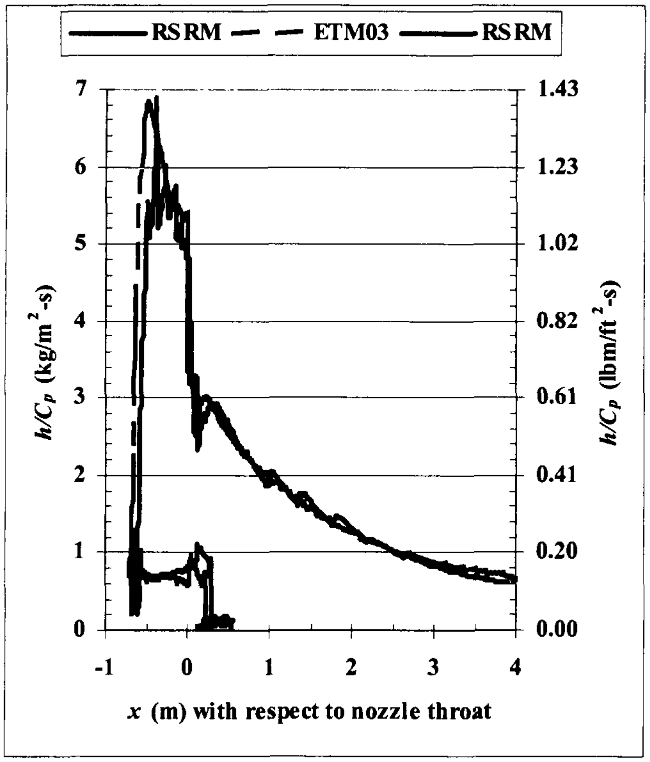

Fig. 9 RSRM and ETM03 wall heat transfer coefficients.

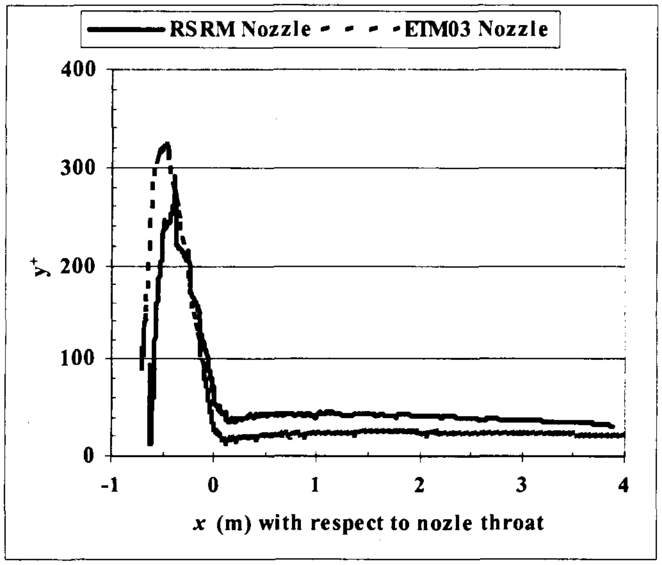

Fig. 11 RSRM and ETM03 nozzle wall y^+.

The following results pertain to slag accretion. Figures 12, 13 and 14 show the RSRM and ETM03 calculated slag rate of accretion flux for six burn times on the aft-dome wall, nozzle nose-cap, and the wall surface starting at the nozzle nose-cap tip to the nozzle throat, respectively. The aft-dome wall is part of the steel case and emerges as propellant burns back. Overall, ETM03 will accrete more slag in comparison with the RSRM. This is expected since the ETM03 mass flow rate is roughly higher than in the RSRM by 20%.

For the RSRM, the integrated values for the Aft-end (absent at 1 s post ignition), Nose-cap, and Nose-cap to throat are calculated to be 770 kg (1698 lbm), 1163 kg (2564 lbm), and 1287 kg (2837 lbm), respectively. For the ETM03, the corresponding integrated values are calculated to be 781 kg (1722 lbm), 1648 kg (3633 lbm), and 1476 kg (3254 lbm), respectively. Summing the above accretions would yield a total of 3220 kg (7099 lbm) and 3905 kg (8609 lbm) for the RSRM and ETM03, respectively. It is interesting to note that the ratio of accretion retained in the ETM03 to the RSRM is thus 1.21 which is consistent with the relative mass flow rate of the ETM03 to the RSRM.

In considering slag retention, the summation of the integrated accretions is limited to the aft-end and nose-cap walls. This is because these are the only areas where slag is likely to accumulate. Slagging from the nozzle nose to throat will most likely be carried out of the motor. This summation yields 1933 kg (4262 lbm) for the RSRM and 2429 kg (5355 lbm) for ETM03. Again, it is interesting to note the ratio of integrated accretion in the ETM03 to RSRM is now 1.26 which is again consistent with the relative mass flow rate of the ETM03 to the RSRM. The ratio of total slag retained along the three surfaces of the ETM03 to the RSRM is shown in Fig. 15. They are 1.01, 1.42, and 1.15 along the aft-dome, nose-cap, and nose-cap to throat, respectively.

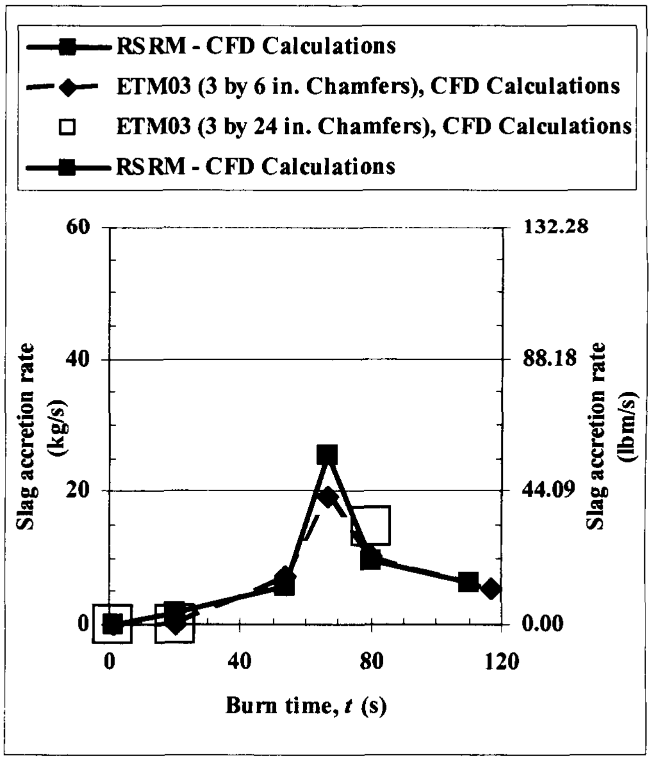

Fig. 12 RSRM and ETM03 slag rates of accretion flux on the aft-dome eroded wall.

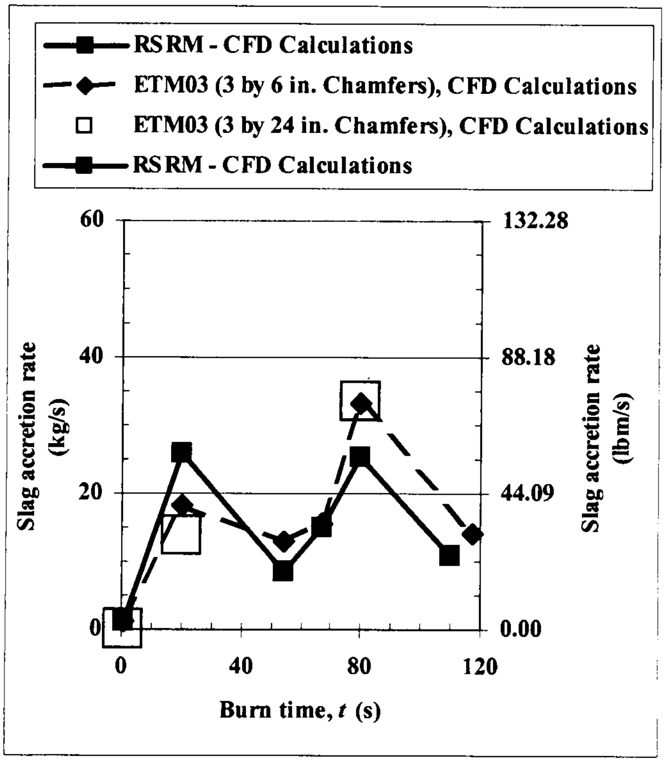

Fig. 13 RSRM and ETM03 slag rates of accretion flux on the nose-cap eroded wall.

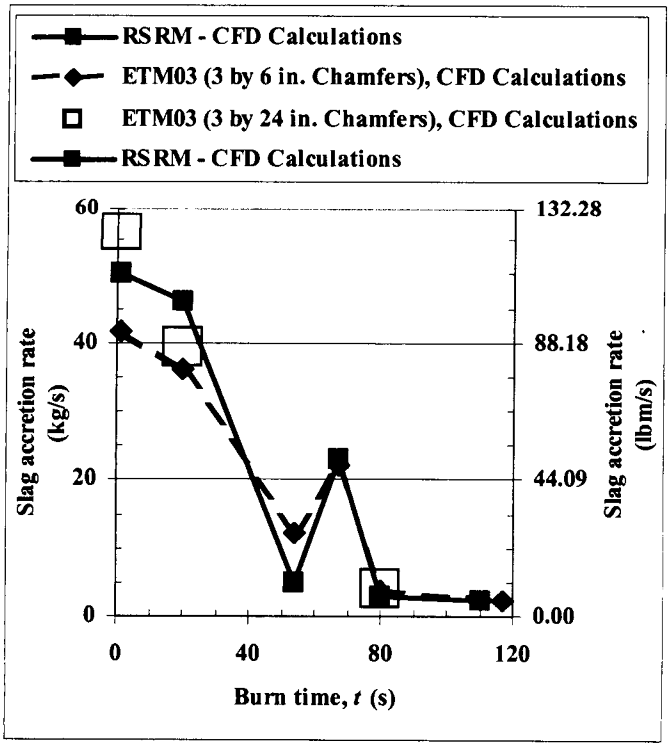

Fig. 14 RSRM and ETM03 slag rates of accretion flux on eroded wall from nose-cap to the nozzle throat.

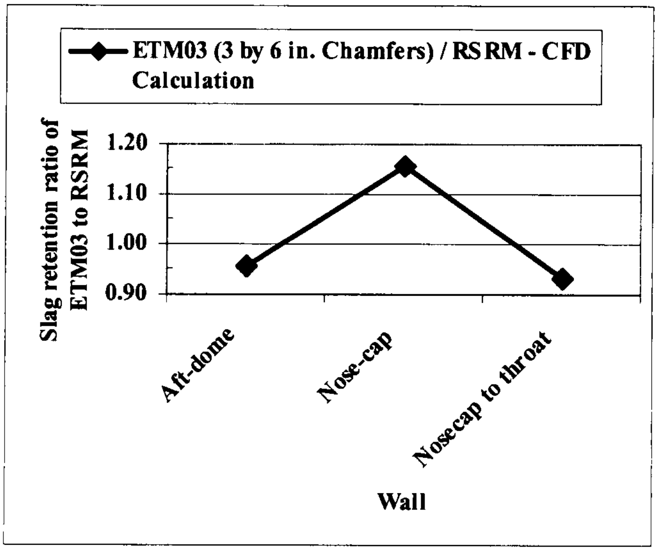

Fig. 15 Slag retained ratio in the ETM03 to the RSRM.

The calculated accretion is shown in Fig. 16 in comparison with statically fired test motors. The CFD predicted values are relatively higher than the maximum retained in static test motors. The current state-of-the-art assumes that particles are trapped as they hit a wall. It does not allow particles to reflect, slide or shatter, etc.

At this time, it is more meaningful to consider the ratio of slag accretion in the ETM03 to the RSRM along the walls (1.01, 1.42, and 1.15) shown in Fig. 15 and as an aggregate ratio of 1.26 for scaling purposes.

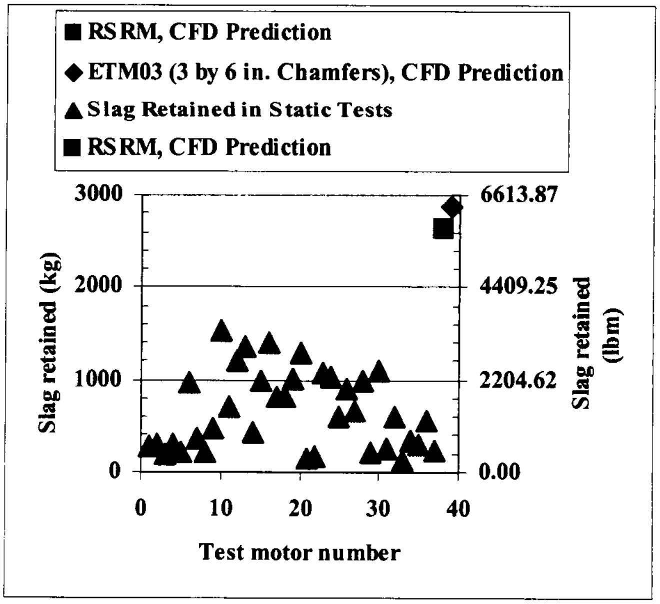

Fig. 16 RSRM and ETM03 slag accretions predicted by CFD in comparison with slag retained in statically fired motors.

Summary and Conclusions

Based on these comparative analyses conducted in this study, the objective of ETM03 will be achieved by providing a more adverse operating environment for motor components than the nominal RSRM environment. For example:

- Higher chamber pressure drop in ETM03 (1.31 MPa (190 psia)) than in RSRM (1.172 MPa (170 psia)).
- Higher centerline Mach numbers approaching the nozzle in ETM03 (0.7) than in RSRM (0.6).
- Higher heat transfer rates for the internal insulation and nozzle components in ETM03 than in RSRM.
- Higher levels of droplet impingement and slag accumulation in ETM03 than in the RSRM.
- Comparisons of ETM03 results for 7.62 by 15.24 cm (3 by 6 in.) and 7.62 by 60.96 cm chamfers (3 by 24 in.) show little change in environment.

References

[1] McBride, B.J., Reno, M.A., and Gordon, S., "CET93 and CETPC: An Interim Updated Version of the NASA Lewis Computer Program for Calculating Complex Chemical Equilibria With Applications," NASA Technical Memorandum 4557, 1994.

[2] GRIDGEN User Manual Version 13" by Pointwise, Inc. 1998.

[3] Gambit Training Notes, TRN-1998-003, Dec. 1998.

[4] TableCurve® 2D V 5.0/3D V 3.0 automated surface fitting software, Jandel Scientific, San Rafael, CA, 1993.

[5] FLUENT 5 Solver Training Notes, TRN-1998-006, Dec. 1998.

[6] McBride, B.J., Reno, M.A., and Gordon, S., "CMA-Charring Material Thermal Response and Ablation Program, SEE01, Version 1.6," Computer Software Management and Information Center (COSMIC), The University of Georgia Office of Computing and Information Services, Athens, Georgia, May 1994.

[7] Brennan, M., "Recent Combustion Bomb Testing of RSRM Propellant," AIAA Paper 96-3270, AIAA/ASME/SAE/ASEE 32nd Joint Propulsion Conference, Lake Buena Vista, FL, July 1-3, 1996.

[8] Whitesides, R.H., Dill, R.A. and Purinton, D.C., "Application of Two-Phase CFD Analysis to the Evaluation of Asbestos-Free Insulation in the RSRM," AIAA-97-2861, AIAA/ASME/SAE/ASEE 33rd Joint Propulsion Conference, Seattle, WA, July 6-9, 1997.